

JGR Space Physics

RESEARCH ARTICLE

10.1029/2019JA027742

Dawnside Auroral Polarization Streams

Jiang Liu^{1,2} , L. R. Lyons¹ , Chih-Ping Wang¹ , M. R. Hairston³ , Yongliang Zhang⁴ , and Ying Zou⁵ 

Key Points:

- Dawnside auroral polarization streams (DAPS) are eastward fast ionospheric flows within the return flow of the dawnside convection cell
- A DAPS is located within the Region 1 current; it has a flow peak and steep flow gradient near the boundary between Region 1 and 2 currents
- A DAPS likely results from enhanced Region 2 current, which occurs during geomagnetically active time

Supporting Information:

- Supporting Information S1
- Data Set S1

Correspondence to:

J. Liu,
jliu@igpp.ucla.edu

Citation:

Liu, J., Lyons, L. R., Wang, C.-P., Hairston, M. R., Zhang, Y., & Zou, Y. (2020). Dawnside auroral polarization streams. *Journal of Geophysical Research: Space Physics*, 125, e2019JA027742. <https://doi.org/10.1029/2019JA027742>

Received 17 DEC 2019

Accepted 1 JUN 2020

Accepted article online 19 JUN 2020

¹Department of Atmospheric and Oceanic Sciences, University of California, Los Angeles, CA, USA, ²Department of Earth, Planetary and Space Sciences, University of California, Los Angeles, CA, USA, ³William B. Hanson Center for Space Sciences, University of Texas at Dallas, Richardson, TX, USA, ⁴The Johns Hopkins University, Applied Physics Laboratory, Laurel, MD, USA, ⁵Department of Space Science, University of Alabama, Huntsville, AL, USA

Abstract Although the postmidnight-to-dawn sector of the auroral ionosphere contains interesting dynamic phenomena that may significantly impact the magnetosphere-ionosphere-thermosphere system, it has been much less studied than the dusk-to-premidnight sector. We discuss a dynamic phenomenon in the postmidnight-to-dawn sector of the auroral oval, eastward fast flows mainly within the expanse of the Region 1 current (its part equatorward of the polar cap). These flows peak and have a steep speed gradient (increase from low to high latitude) near the interface between the Region 1 and Region 2 currents. Because such flows correspond to an electric field that most likely comes from enhanced Region 2 currents and an associated spatial conductivity gradient, their generation mechanism is analogous to that of a subauroral polarization stream. Therefore, we refer to such an eastward flow as a dawnside auroral polarization stream (DAPS). We show several examples of the presence and absence of DAPS under different geomagnetic activity levels. A DAPS' electric field can heat the ionosphere (and thus the thermosphere), change the convection pattern of the magnetosphere-ionosphere system, and modify the drift path of magnetospheric particles. Because a DAPS' flow peak maps to a major site of magnetic-kinetic energy conversion in the magnetosphere (the transition region between dipole and stretched field), it may be important for the conversion. A DAPS' steep flow gradient is also potentially important; it may lead to instabilities, such as that responsible for auroral Omega bands. Given its potential importance, knowledge of DAPS is fundamental for understanding the magnetosphere-ionosphere-thermosphere system.

Plain Language Summary Phenomena in Earth's magnetosphere (thousands of kilometers to hundreds of thousands of kilometers away from Earth's surface) lead to plasma flows in Earth's ionosphere (hundreds of kilometers above Earth's surface). Ionospheric properties modify these flows, which in turn feed back to the magnetosphere and result in other activities there. Ionospheric flows significantly affect ionospheric electric field, currents, and temperature, which greatly impact telecommunication, navigation, and power grids. We discuss one type of ionospheric flow that has been largely overlooked in previous studies and propose a generation mechanism for it. This type of flow may be crucial in magnetospheric plasma circulation, ionospheric heating, and energy transport in the magnetosphere-ionosphere system.

1. Introduction

Dynamical processes in Earth's nightside auroral oval reveal phenomena along plasma sheet magnetic field lines. Understanding the conditions responsible for these processes helps us understand the nightside magnetosphere-ionosphere (M-I) system. Previous studies of dynamic processes in the nightside auroral oval (e.g., Nishimura et al., 2010; Zou, Lyons, Wang, et al., 2009) tended to focus on the dusk-to-premidnight sector because many dynamic structures related to substorms, one of the most important energy conversion processes in the magnetosphere (e.g., Akasofu, 1964), have been observed there. Although half of the convection in the plasma sheet occurs there, the postmidnight-to-dawn sector of the auroral oval has received significantly less attention. Because that sector (i.e., within the dawnside convection cell) is less perturbed by small-scale dynamic structures than the dusk-to-premidnight sector, it is ideal for studying the large-scale variation of the M-I system during active times.

The M-I system is coupled through electric fields. As a result, bulk plasma flows in the magnetosphere and ionosphere (above the E region) “map” to each other (e.g., Maynard et al., 1995; Wolf, 1970). The nightside

magnetosphere contains tailward flows in the open magnetic flux region, earthward flows in the plasma sheet, and vanishingly small (compared with flows in the plasma sheet) azimuthal flows (with an earthward component) in the inner magnetosphere (Dungey, 1961). When mapped to the postmidnight-to-dawn sector of the ionosphere, these flows correspond to antisunward flow (with a westward component) in the polar cap, eastward flow in the auroral oval (the ionospheric footprint of the plasma sheet), and vanishing flow equatorward of the oval (e.g., Foster, 1983; Heppner, 1977). During weak, steady convection, the east-west component of the ionospheric flow should vary smoothly with latitude—monotonically change from westward in the polar cap to an eastward peak at the middle of the auroral oval, and then decrease monotonically to a vanishing value equatorward of the oval (e.g., Evans et al., 1980). The electric field follows the same profile, with poleward (equatorward)-pointing field corresponding to a westward (eastward) flow ($\mathbf{E} = -\mathbf{V} \times \mathbf{B}$). According to Equation A4 in the Appendix, the electric field profile from the polar cap to its peak in the middle of the oval (from the peak to the low-latitude edge of the oval) requires a downward (upward) field-aligned current (FAC). This statement assumes that the Pederson conductivity does not vary too much inside the oval. The downward and upward FACs are Region 1 and 2 (R1 and R2) currents, respectively (Iijima & Potemra, 1976). Thus, the eastward flow naturally peaks near the boundary between R1 and R2 current. Such flow peaks near the boundary have been termed Birkeland current boundary flows (BCBFs) (Archer et al., 2017).

Sometimes, an eastward BCBF in the postmidnight-to-dawn sector deforms to the following latitudinal profile: in the lower-latitude part of the auroral oval, the flow is much smaller than that in the higher-latitude part, and it increases over latitude with a steep gradient (within $\sim 0.1^\circ$ from a small value to its peak. See, e.g., the orange trace in Figure 2 of Archer et al., 2017; although they did not mention the local time of their observation, we can infer from the magnetic field variation that it was in the postmidnight-to-dawn sector). The flow peak is usually larger than ~ 1 km/s. As we will demonstrate in the next section, such eastward fast flow likely results from the same process that gives rise to subauroral polarization streams (SAPS) (Foster & Vo, 2002; Galperin et al., 1973; Spiro et al., 1979). Because of this relationship to the SAPS process, we refer to such flows as dawnside auroral polarization streams (DAPS). As it is a fast flow, a DAPS may impact the magnetosphere-ionosphere-thermosphere (M-I-T) system as the SAPS does; furthermore, its flow gradient may cause instabilities in the system. Thus, it is important to understand when and how DAPS arise.

2. A Possible Generation Mechanism of DAPS

A DAPS-like flow appeared in the Rice-Convection Model (RCM) simulation by Gkioulidou et al. (2009). The flow was not discussed in that paper, but by understanding this simulation, we can understand the nature of DAPS. In Figure 1 we explain a plausible generation mechanism of DAPS based on that simulation.

When convection in the magnetosphere and the ionosphere enhances from quiet time, equatorward ionospheric flows extend to low latitudes (compare the flow lines in active-time Figure 1b to those in quiet-time Figure 1a). Thus, at an early stage of active time (i.e., Figure 1b), enhanced convection can bring particle flux farther earthward than the quiet-time convection can. After the convection has remained at an enhanced level for some time, the plasma sheet pressure increases (Figure 1c). This pressure buildup enhances R2 FACs in the magnetosphere and ionosphere (R2 FACs; toward/away from the ionosphere in the dusk/dawn sector of the tail; Figures 1d and 1e). Horizontal ionospheric currents (perpendicular to the magnetic field) must change to maintain continuity with the enhanced R2 FACs, which in turn requires that the spatial distributions of ionospheric electric field, and thus flows, be modified. Equatorward of the R2 current, this modification shields the low-latitude ionosphere from convection flows—i.e., it cancels the lower-latitude north-south flows in Figure 1b (comparing Figure 1e to 1b, subauroral streamlines are farther away from each other; see also Jaggi & Wolf, 1973). Within the R2 current and poleward of it, the modified electric field enhances east-west convection. Effectively, the electric fields required by the enhanced R2 current shift streamline alignment from north-south to east-west. In the dusk convection cell, the modified electric field leads to a well-known SAPS (Foster & Vo, 2002) and a Harang (1946) reversal (Figure 1f).

In the dawn convection cell (covering the postmidnight-to-dawn sector), the modified electric field leads to the topic of this paper, DAPS. In this convection cell, the enhanced R2 FAC is upward, so it must be fed by a north-south Pederson current from higher and/or lower latitudes (see Equation A4 in Appendix). Equatorward of the R2 current, electric field, and thus Pederson current, nearly vanishes because of the

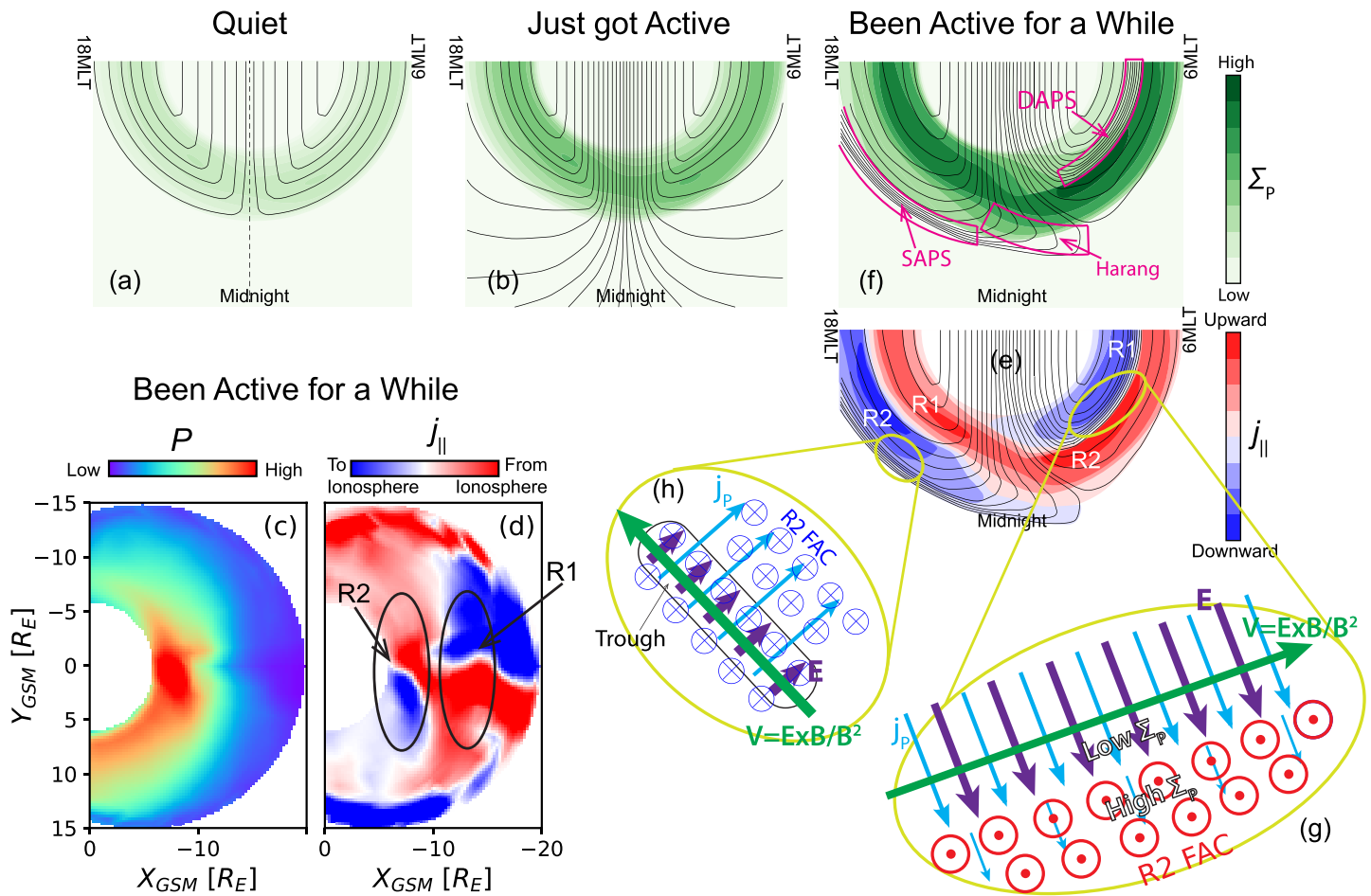


Figure 1. Suggested generation mechanism of DAPS (schematics), based on the simulations of Gkioulidou et al. (2009) and Wang, Gkioulidou, et al. (2018). Conditions in the high-latitude ionosphere: (a) quiet, (b) convection has just got enhanced, (e–f) convection has been active for a while (e.g., >30 min). Conditions in the magnetosphere: (c, d) convection has been active for a while. The black curves are equipotential lines, approximating streamlines of plasma flow. The height-integrated Pederson conductivity, Σ_p , is shown in panels (a), (b), and (f). The thermal pressure, P , is shown in panel (c) and FAC density, $j_{||}$, is shown in panels (d) and (e) (positive toward the ionosphere). (g) Schematics illustrating DAPS (green arrow), Pederson current j_P (light blue arrows), and electric field (purple arrows). (h) Schematic illustrating SAPS (green arrow; to better understand this schematic, please see Anderson et al., 1993).

shielding effect. Thus, the predominant supplier of the enhanced R2 current must be enhanced Pederson current flowing toward it from higher latitudes (Figure 1g), which can be supplied by the also-enhanced R1 FAC (downward) during active time (Figures 1d and 1e). The enhanced Pederson current requires an enhanced equatorward electric field ($\mathbf{J}^P = \Sigma_p \mathbf{E}$) and thus an eastward fast flow ($\mathbf{V} = \mathbf{E} \times \mathbf{B}/B^2$) parallel to the boundary between R1 and R2 FACs (Figure 1g and the dense streamlines inside the white box in Figure 1e). The enhanced R2 FAC has a steep poleward boundary (i.e., the upward FAC density is large very close to the boundary; see Figure 1e) due to considerable pressure buildup in the tail. According to Equation A4, the Pederson current, and thus the equatorward electric field and eastward flow, should also show a significant gradient near the poleward boundary of the R2 current.

The equatorward electric field (and thus the eastward flow) can be further enhanced by conductivity distribution. Because it is an upward FAC (downward electrons hitting the ionosphere), the enhanced R2 current creates high conductivity in the lower-latitude part of the auroral oval (where the R2 current is); this conductivity is much higher than that in the region poleward of the R2 current (Figure 1f). This high conductivity suppresses electric fields in the entire latitudinal width of the R2 current because any significant electric field will lead to a Pederson current too large to close. As a result, the lower conductivity region poleward of the R2 current (the latitudinal range of R1 current within the auroral oval) needs a stronger electric field to complete the potential drop across the convection return-flow region (i.e., the auroral oval; see also Jiang

et al., 2015). Strong electric field is a common feature of low conductivity regions that are adjacent to high conductivity regions (e.g., Baumjohann, 1982; Marklund et al., 1982; Ziesolleck et al., 1983); such electric field is termed “polarization electric field” (e.g., Marklund, 1984). Because the enhanced R2 current has a steep poleward boundary (Figure 1e), the conductivity also has a steep gradient at the boundary between R1 and R2 currents. This conductivity gradient will lead to a steep gradient in the equatorward electric field and thus the eastward flow—the flow poleward of the boundary (within the R1 current) will be much faster than that equatorward of it (within the R2 current; see Figures 1e and 1f).

Because the eastward fast flow is located within the auroral oval and is associated with a strong electric field, we refer to it as a DAPS. It is clear from Figure 1 that the generation of DAPS is analogous to that of SAPS (see, e.g., Anderson et al., 1993; and Gkioulidou et al., 2009 for proposed SAPS generation mechanisms). Both SAPS and DAPS result from the electric field required by enhanced R2 current and appear in low conductivity regions. The SAPS arises when the Pederson current required by the R2 current flows inside the midlatitude trough (Muldrew, 1965; Sharp, 1966), one of the lowest conductivity regions near the auroral zone (Figure 1h), whereas DAPS arises where the conductivity is relatively very low compared to its immediate neighbor, the enhanced R2 current (see section 5.1.3 for more discussion).

In the DAPS generation mechanism of Figure 1, ionospheric electric field needs to adjust itself with conductivity, so the resultant Pederson current is always big enough to guarantee current continuity with the FAC from the magnetosphere. Thus, the magnetospheric process responsible for DAPS acts as a “current generator” (e.g., Nishida, 1979), which is the usual case for ionospheric structures with similar spatial scales to DAPS (Vickrey et al., 1986). The DAPS generation mechanism should apply to all local times where the tail pressure buildup is effective and the R2 current is upward. These include 0–6 MLT (magnetic local time), so we expect DAPS to appear there.

In addition to the increased overall convection in Figure 1, another possible driver of DAPS is a bursty bulk flow (BBF), an earthward fast flow channel in the plasma sheet (Angelopoulos et al., 1992). Each BBF comprises one to several flow bursts associated with entropy-depleted flux tubes termed plasma bubbles (Pontius & Wolf, 1990) or dipolarizing flux bundles (Liu, Angelopoulos, Runov, et al., 2013; Liu et al., 2014). Each BBF has a small dawn-dusk width of 0.5–3 R_E (Liu, Angelopoulos, Zhou et al., 2013; Sergeev et al., 1996). BBFs have been suggested to enhance plasma sheet pressure, R2 currents, and SAPS (e.g., Birn & Hesse, 2013; Gallardo-Lacourt et al., 2017; Liu, Angelopoulos, Zhou, et al., 2013), so we expect BBFs to also enhance DAPS. Supporting this idea, the Rice Convection Model simulation of BBFs produced magnetospheric dawnward flows whose ionospheric counterpart should be DAPS (see Figure 7c of Wang, Gkioulidou, et al., 2018).

Because DAPS and SAPS have a common origin, DAPS may play a role as significant as that of SAPS in the M-I-T system. The DAPS' electric field should significantly heat the ionosphere and thermosphere and may thus significantly modify ionospheric and thermospheric properties (e.g., temperature, density, and recombination rate). It will also substantially change the potential distribution of the M-I system, which determines convection and drift paths of energetic particles.

Ionospheric flows that are likely DAPS have been observed before (Aikio et al., 2018; Ziesolleck et al., 1983) and explained to be caused by enhanced upward FAC and conductivity equatorward of the flow (Brüning et al., 1985; Brüning & Goertz, 1986). However, the relative location of these previously observed flows to the large-scale R1 and R2 currents is unknown, so it is unclear whether they are indeed DAPS. Therefore, the importance of DAPS as part of the large-scale M-I system has not been well understood. As a first step to achieving this understanding, we examine several DAPS events in detail.

3. Data Set

The most direct identification of DAPS comes from measurements of ionospheric plasma flow. We will use such measurements from two missions—DMSP (Defense Meteorological Satellite Program) and Swarm. All DMSP and Swarm spacecraft have polar orbits, so when they transect the auroral zone, their moving direction and cross-track direction (perpendicular to the direction of spacecraft motion and in the horizontal plane) are approximately north-south and east-west aligned, respectively. The DMSP mission consists of spacecraft with ~840 km altitude in the ionosphere's *F* region. The newer DMSP spacecraft are equipped

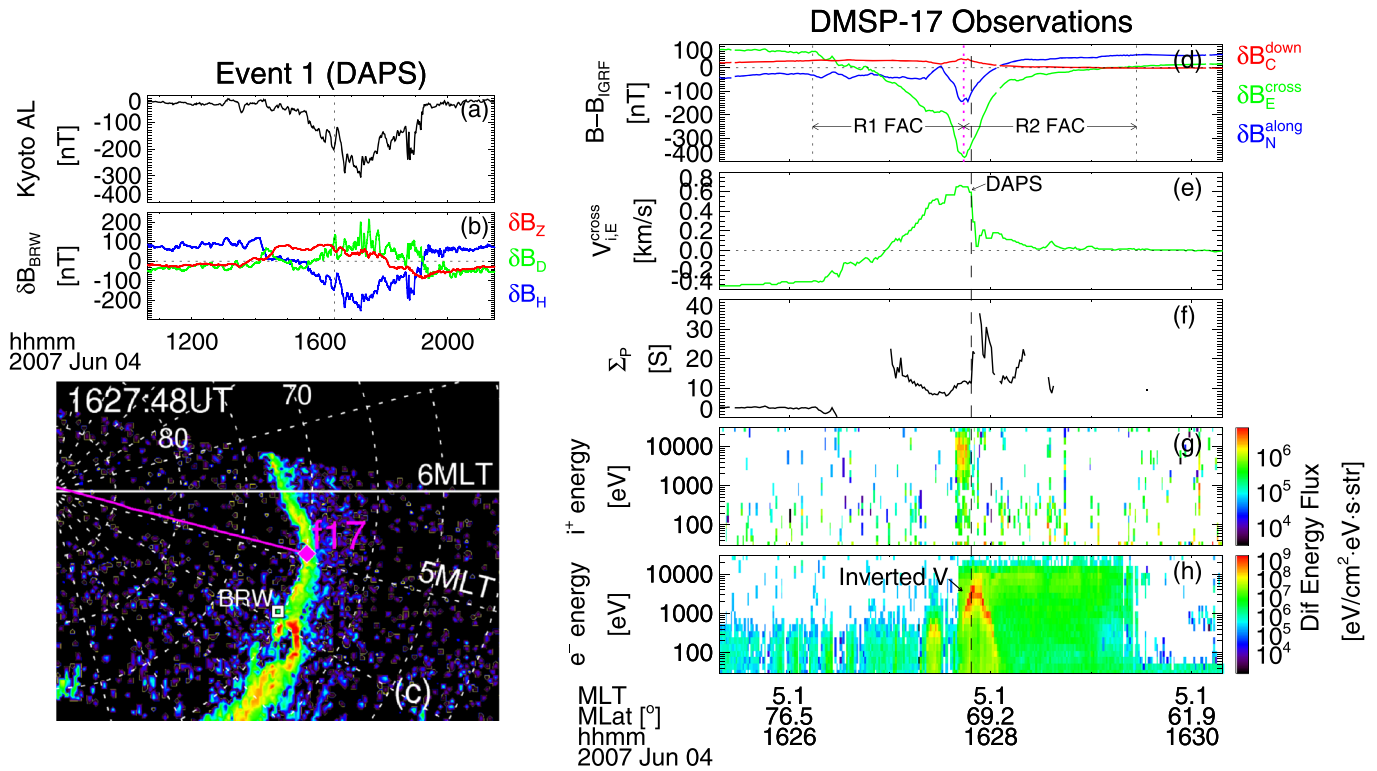


Figure 2. DMSP observation of a DAPS event. (a) AL index. (b) Ground magnetometer observation (the average field of the plot range has been subtracted) at Barrow (its location is represented by a white square in panel (c)). Vertical dotted line = the time of the event. (c) Ultraviolet auroral emissions from SSUSI. Redder color = more intense light flux. All SSUSI images presented in this paper have the same color scale. Dashed grids = magnetic latitudes and MLTs. Magenta line and diamond = spacecraft track and location, respectively (both projected to 110 km altitude), at the time in the auroral image. (d–h) DMSP in situ measurements; the vertical dashed line marks the time of panel (c). (d) δB , the magnetic field after subtracting IGRF. $\delta B_E^{\text{cross}}$ (green; positive eastward) and $\delta B_N^{\text{along}}$ (blue; positive northward) are in the horizontal plane and perpendicular and parallel, respectively, to the spacecraft track. δB_C^{down} (red) points vertically down when positive. Vertical dotted lines = ranges of the R1 and R2 currents. Magenta line = R1/R2 boundary. (e) Cross-track ion bulk flow (in the horizontal plane and perpendicular to spacecraft trajectory; positive eastward). (f) Height-integrated Pederson conductivity (data gaps are where the requirements for computing it is violated; see Appendix A). (g and h) Differential energy flux of precipitating ions and electrons.

with ion drift sensors that can measure ion bulk flows in the cross-track and vertical directions (e.g., Rich & Hairston, 1994). The Swarm mission consists of three identical spacecraft, and this paper presents data from Swarm-A, which has a ~460 km altitude. Each Swarm spacecraft is equipped with a set of thermal ion imagers (TII), which are part of the electric field instrument (EFI) (Knudsen et al., 2017). The TII measures ion bulk flows' cross-track and vertical components. Although we should view the absolute values of the measured flow with caution, the flow's profile (i.e., the shape of the flow curve when plotted as function of time; see, e.g., Figure 2e) and variation are reliable (see validations by Lomidze et al., 2019). Because the flow data used in this study may suffer from offset, we subtract the average measured velocity within an unperturbed latitude range equatorward of the R2 FAC (we expect the flow in such ranges to vanish) (Archer et al., 2017; Liu et al., 2018; Lomidze et al., 2019).

In all the DMSP and Swarm spacecraft whose data are presented in this paper, boom-mounted fluxgate magnetometers are on board to measure the in situ magnetic field vector (Merayo et al., 2008; Rich, 1984). Each DMSP spacecraft can measure the precipitation of 30 eV–30 keV plasma (see Hardy et al., 2008, and references therein).

To understand the context of the in situ measurements of ionospheric plasma, we also consider the AL (Auroral-Low) index, ground magnetometer measurements from the SuperMAG network (Gjerloev, 2009, 2012), and auroral images from THEMIS All-Sky Imagers (ASIs) (Mende et al., 2008) and DSMP's ultraviolet spectrographic imager (SSUSI) (Paxton et al., 2018). When a spacecraft flies over the field of view (FOV) of an auroral imager (DMSP is always over SSUSI's FOV because the imager is onboard

Table 1

A Summary of the Events we Present in This Paper

Event	DAPS?	Date	Field/flow observed by	Aurora observed by	Presented by figure	Explained in section
Event 1	Yes	June 4, 2007	DMSP-17	SSUSI	2	4.1.1
Event 2	Yes	April 11, 2009	DMSP-17	SSUSI	3	4.1.2
Event 3	Yes	August 22, 2014	Swarm-A	THEMIS ASI	4	4.2
Event 4	No	April 19, 2013	DMSP-16	SSUSI	5	4.3.1
Event 5	No	May 13, 2013	DMSP-16	N/A	6	4.3.1
Event 6	No	January 1, 2016	Swarm-A	N/A	7	4.3.2

Note. Dates are presented in the format of month/day/year.

DMSP), we can compare their measurements. To compare them more accurately, we will map each spacecraft's location to an assumed auroral altitude of 110 km. We use this altitude value because it is where most electrons deposit their energy in the ionosphere, generating aurorae, and it has been commonly used for auroral altitude in previous studies.

To summarize, the data presented in this paper are from various missions: ionospheric field and flow data come from DMSP or Swarm (depending on event), precipitation data comes from DMSP, aurora luminosity comes from DMSP-SSUSI or THEMIS ASI (depending on event), and ground magnetic field comes from SuperMAG magnetometers.

4. Case Studies

We present several observations of ionospheric plasma bulk flows by DMSP or Swarm (the events are listed in Table 1). For events with auroral images available, the main auroral arcs are approximately perpendicular to the direction of spacecraft motion (the east-west direction). Under this condition, the R1 and R2 FAC sheets, which are parallel to the main arc, are approximately parallel to the spacecraft's cross-track direction. Because we expect the DAPS to be parallel to the boundary between R1 and R2 current sheets (see Figure 1f), this condition is optimal for the cross-track flow measurement to capture a DAPS signature.

4.1. DAPS in Active Time

Consistent with the mechanism shown in Figure 1, we found DAPS during geomagnetically active times.

4.1.1. Event 1

Figure 2 presents an event observed by DMSP-17 around 1628 UT on 4 June 2007 (Event 1). Around this time, the AL index is dropping from approximately -50 nT to a minimum of approximately -330 nT, indicating a substorm expansion phase (Figure 2a). At 1627:50 UT, the equatorward-moving DMSP-17 passes the poleward boundary of a bright discrete arc and enters the arc at ~ 5.1 MLT (Figure 2c). Poleward of this boundary, the eastward component of the ionospheric magnetic field (δB_E , the green curve in Figure 2d; Earth's dipole field has been subtracted) shows a gradual drop with decreasing latitude (from 1626:14 to 1627:44 UT). This drop corresponds to an east-west aligned, downward FAC sheet (e.g., Iijima & Potemra, 1976). Equatorward of the boundary, δB_E increases with decreasing latitude (from 1627:44 to 1629:27 UT), indicating an east-west aligned, upward FAC sheet. These neighboring downward and upward FAC sheets are R1 and R2 currents, respectively. The locations of the currents have corresponding precipitation signatures—ions show strong precipitation at 1627:42 UT (Figure 2g) coinciding with a steep δB_E drop in Figure 2d that indicates a narrow, intense downward FAC. Thus, this narrow downward FAC is likely related to a localized ion pressure gradient in the plasma sheet (see Figure 1c). As expected, the latitudinal width of the R2 current coincides with enhanced electron precipitation (green to yellow color in Figure 2h). The intense part of the R2 current (the steep δB_E increase from 1627:44 to 1628:11 UT in Figure 2d) corresponds to an inverted-V structure in Figure 2h and the bright arc in Figure 2c, as expected (e.g., Lyons, 1981).

Figure 2e shows the eastward cross-track flow. A prominent eastward fast flow appears immediately poleward of the R2 current, with a steep gradient (covering $\sim 0.1^\circ$ latitude; the vertical dashed line) near the boundary between the R1 and R2 currents (i.e., the minimum δB_E point as indicated by the magenta vertical dotted line in Figure 2d; the gradient is $\sim 0.4^\circ$ equatorward of this boundary) and in the middle of the inverted

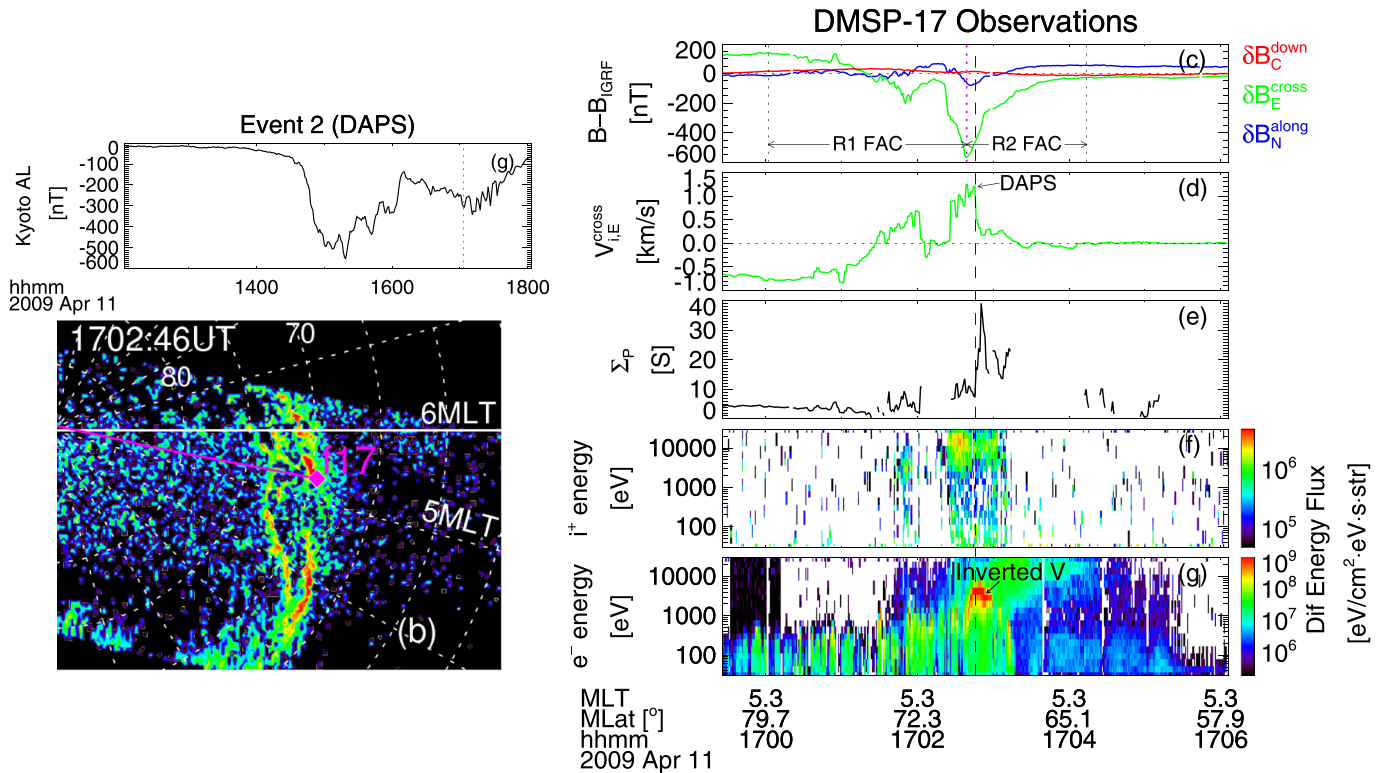


Figure 3. DMS-17 observation of another DAPS event, ordered in a similar way to Figure 2 (except not showing ground magnetometer observations).

V structure. These signatures are consistent with the DAPS signatures predicted in Figure 1. Therefore, we refer to the strong flows around the flow peak in Figure 2e as a DAPS. Dividing δB_E by the eastward flow speed, we estimate the height-integrated Pederson conductivity in Figure 2f (see the Appendix A for the details of this method). The conductivity has a steep gradient at the boundary between the R1 and R2 currents—it is high at the poleward portion of the R2 current. The high conductivity region coincides with the intense R2 current (1627:44 to 1628:11 UT in Figure 2d), the bright arc, and the inverted-V precipitation. That these are all immediately equatorward of the flow peak is consistent with our suggested cause of DAPS.

Figure 2b presents ground magnetic field variations at Barrow around the time of the DAPS observation. During the substorm from ~1534 to ~1918 UT (i.e., the interval of low AL in Figure 2a), the Barrow magnetometer measures southward variation (i.e., negative B_H change in Figure 2b). This is caused by the westward electrojet (e.g., Wiens & Rostoker, 1975), a Hall current caused by southward electric fields in both the bright arc and the dark region immediately poleward of the arc. The southward electric field in the dark region is responsible for DAPS. When DMS-17 observed the DAPS (vertical dotted line in Figure 2b), the Barrow magnetometer sits at the poleward boundary of a bright discrete arc, where DAPS is expected (Figure 2c). The measured field in Figure 2b shows an eastward peak (i.e., positive B_D peak) at the time of DAPS observation. This eastward peak must result from the southward Pederson current associated with the aforementioned southward electric field, because the only other currents causing B_D change, the R1 and R2 FACs, should lead to a westward B_D at Barrow. That the eastward B_D variation is a peak suggests that the Pederson current is enhanced, as expected from DAPS. The enhanced Pederson current is strong enough to overcome the impact of R1 and R2 FACs on B_D .

4.1.2. Event 2

Figure 3 presents a DAPS event around 1703 UT, on 11 April 2009 (Event 2). During this time, AL is ≤ 200 nT and decreasing. Two hours before, AL reached approximately -550 nT. Event 2 is thus likely observed during the expansion phase of a secondary substorm after a major substorm. Because this event has more active preconditioning than Event 1, the auroral image of Figure 3b displays more structures than Figure 2c.

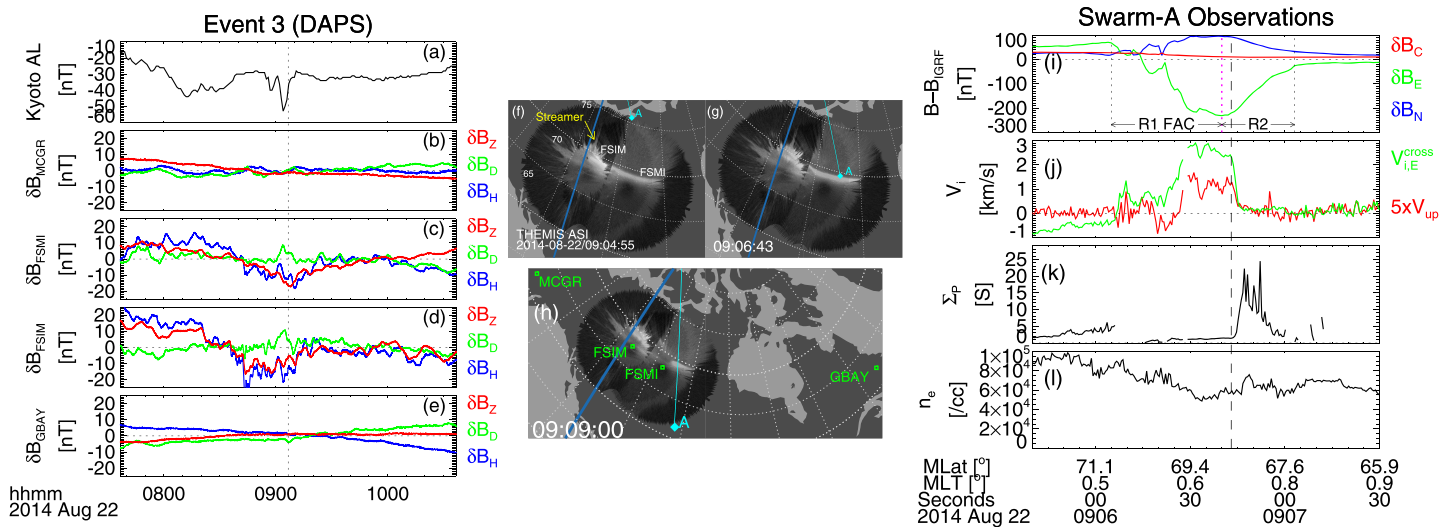


Figure 4. A DAPS event observed by Swarm-A. (a) AL index. (b–e) Ground magnetometer observations (the average field of the plot range has been subtracted) at McGrath, Fort Smith, Fort Simpson, and Goose Bay (their locations are represented by green squares in panel (h)). The vertical dotted line indicates the time of the event. (f–h) Auroral observations from THEMIS ASIs. Dotted lines = invariant latitudes and longitudes. Black areas = obstacles in the imager’s field of view. Dark blue line = midnight. The cyan diamond and line are the footprints of Swarm A and its trajectory, respectively (projected to 110 km altitude). Swarm measurements: (i) δB , the same as Figure 2d except for a different coordinate system: geographic northward (N), eastward (E), and downward (C). (j) Ion bulk flow: cross-track flow (green, positive eastward) and upward flow multiplied by 5 (red). (k) Height-integrated Pederson conductivity. (l) Local electron density. The vertical dashed line in panels (i)–(l) marks the time of panel (g).

Although Figure 3b is noisy, we can still see that by 1702:46 UT, the equatorward-moving DMSP F-17 at ~ 5.3 MLT has passed a bright discrete arc and entered a second even brighter arc. The two arcs are associated with two pairs of downward and upward FACs indicated by decrease and increase of δB_E in Figure 3c. The higher-latitude pair from 1701:31 to 1702:13 UT contains a much smaller amount of FAC (for either upward or downward FAC) than the lower-latitude pair from 1702:21 to 1704:14 UT, as seen by the variation of δB_E magnitude being much smaller. The upward FACs of the weaker and stronger FAC pairs correspond to the higher-latitude minor bright arc and lower-latitude major bright arc in Figure 3b, respectively. We treat the higher-latitude arc and its corresponding FAC pair as a secondary arc embedded in the large-scale R1 current. The intense downward FAC (steep δB_E drop from 1702:31 to 1702:38 UT in Figure 3c) at $\sim 1702:34$ UT coincides with enhanced ion precipitation (Figure 3f; this also is the case for the downward current associated with the higher latitude arc and for Event 1, suggesting a possibly interesting topic for future study). As for Event 1, the R2 upward FAC in this event corresponds to enhanced electron precipitation (Figure 3g). Also, inverted-V electron precipitation expectedly appears at the time of the intense upward FAC (steep δB_E increase from 1702:39 to 1702:53 UT in Figure 3d) and the major bright arc which DMSP-17 has entered in Figure 3b.

Figure 3d shows two eastward fast flows (~ 1702 and $\sim 1702:40$ UT), with the lower-latitude flow faster (1.3 km/s) than the higher-latitude one. Each flow has a steep gradient (covering $\sim 0.3^\circ$ latitude) near the boundary between the downward and upward FACs (the magenta dotted line in Figure 3c; the gradient is $\sim 0.5^\circ$ equatorward of this boundary). The lower-latitude fast flow has its gradient near the poleward boundary of the R2 current, so this flow satisfies the definition of a DAPS. Associated with this DAPS is an intense upward FAC (steep δB_E increase at $\sim 1702:34$ UT in Figure 3c) and a high-conductivity region (Figure 3e; coincident with a bright arc in Figure 3b and an inverted-V precipitation in Figure 3g) immediately equatorward of the flow, consistent with the generation mechanism in Figure 1. The higher-latitude flow is also associated with an upward FAC and a discrete arc, so it should have arisen from a mechanism like DAPS. We do not further discuss this flow because its associated FACs (a secondary pair of downward and upward FACs in addition to the R1/R2 currents) is not a common feature of the auroral zone.

Events 1 and 2 demonstrate that DAPS can appear during typical active conditions when the M-I convection is greatly enhanced.

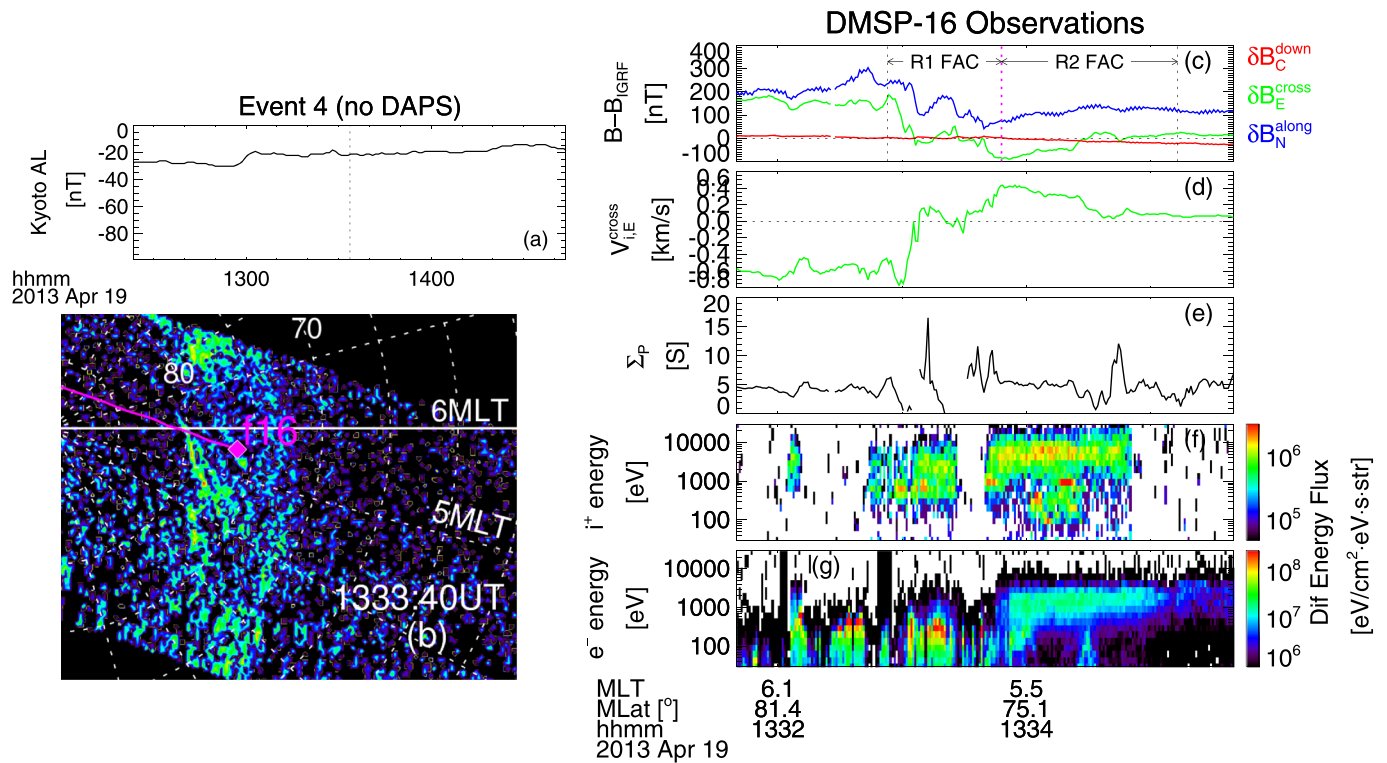


Figure 5. DMS-16 flying over the dawnside auroral zone without a DAPS. Ordered in the same way as Figure 3.

4.2. DAPS in Relatively Quiet Time

Dawnside auroral polarization streams can also appear when the geomagnetic condition is relatively quiet. Figure 4 presents an event during such a time (Event 3). The AL index in Figure 4a shows that around the time of this event (the vertical dashed line at ~0907 UT), AL was only approximately -40 nT. Even though the activity level is so low, Swarm-A still encountered a bright arc when it moved equatorward (Figure 4g). At the time of the encounter, Swarm-A was 0.5 hr of MLT east of midnight. It is within the dawn convection cell because it observed only two major FAC sheets—a downward R1 FAC from 0906:05 to 0906:40 UT (δB_E decrease with decreasing latitude in Figure 4i) and an upward R2 FAC from 0906:40 to 0907:03 UT (δB_E increase in Figure 4i). About 0.1° equatorward of the boundary between R1 and R2 currents (the magenta dotted line in Figure 4i) is a steep flow gradient ($\sim 0906:44$ UT; covering $\sim 0.1^\circ$ latitude), poleward of which is an eastward fast flow (>2.5 km/s) within the low-latitude part of the R1 current (0906:21–0906:45 UT; green trace in Figure 4j). This flow is a DAPS. At the same latitude range of the DAPS, the upward ion flow is enhanced (red trace in Figure 4j) and the plasma density is lower than regions out of the DAPS. Immediately equatorward of the DAPS is a high conductivity region (0906:45–0906:57 UT) associated with the bright arc in the auroral images. The location of DAPS has a low conductivity (Figure 4k), consistent with the theory of Figure 1.

To understand why DAPS can still exist at this relatively quiet time, we revisit the AL index in Figure 4a, which shows a perturbation from 0901:20 to 0908:20 UT with a minimum of approximately -55 nT. This minimum is only ~ 2 min before Swarm-A observed the DAPS. To find the locations where geomagnetic perturbations contributed to the AL perturbation, we plot the field observation by ground magnetometers in Figures 4b–4e (their locations are illustrated in Figure 4h). The most significant magnetic perturbation occurred at Fort Simpson and Fort Smith (Figures 4c and 4d), and the perturbations were minor at McGrath (Figure 4b) and Goose Bay (Figure 4e), which are west and east of the location of the most significant perturbations, respectively. Thus, the magnetic perturbations were localized near Fort Simpson and Fort Smith. Localized perturbations are usually associated with an auroral streamer (e.g., Lyons et al., 2012), the footprint of a BBF channel in the plasma sheet (e.g., Nakamura et al., 2001; Wang, Xing, et al., 2018).

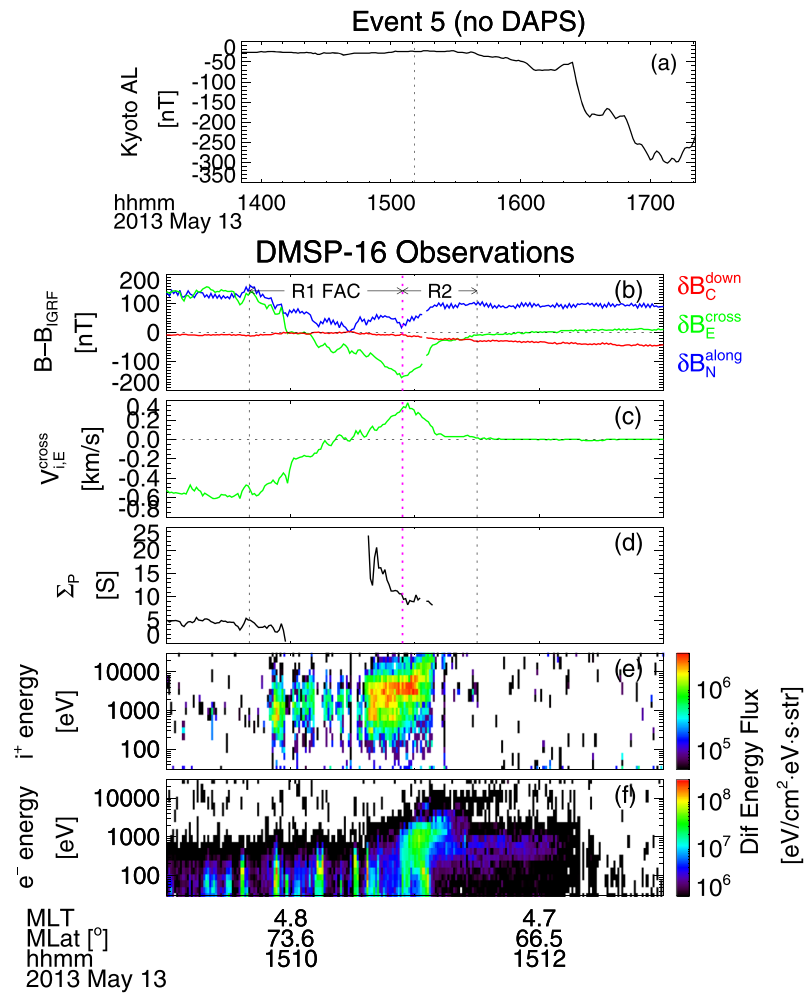


Figure 6. DMSP flying over the dawnside auroral zone without a DAPS. Ordered in the same way as Figure 3, except that SSUSI image is unavailable for this interval.

Around the time of the significant magnetic perturbation, a bright aurora form appears poleward of the main bright arc. This auroral form, likely a streamer (Figure 4f), propagates equatorward (see supporting information Movie S1; from 0902 to 0905 UT), as expected for a streamer whose magnetospheric counterpart is an earthward-propagating BBF. As mentioned in section 2, a BBF should lead to a DAPS because it can enhance R2 current. The enhanced R2 current is indicated by the bright arcs in Figures 4f and 4g (also see Movie S1; from 0902 to 0906 UT). The streamer’s influence is only temporary, so the arc has largely dimmed by 0909 UT (Figure 4h), indicating a weakening R2 current.

4.3. Absence of DAPS

A DAPS is not a constant feature of the postmidnight-to-dawn sector of the ionosphere. In the following we present three cases when DAPS is absent.

4.3.1. Absence of DAPS When the Geomagnetic Activity Level is Low

As suggested by the mechanism in Figure 1, DAPS should be unclear or absent when convection is weak and BBFs are absent, which happens when the geomagnetic activity level is low. When the level is extremely low, it is difficult to even determine the ranges of R1 and R2 currents, so DAPS cannot be defined. During some low activity intervals, we can still determine these ranges. Figure 5 displays one such interval on 19 April 2013 (Event 4), when DMSP-16 transects the auroral zone from ~5.5 MLT. Figure 5a shows that the AL index is approximately -20 nT over the 2 hr around the time of interest (~1334 UT), indicating a very quiet condition. The auroral zone contains several dim, discrete arcs (dim compared to the major discrete arcs in Figures 2b and 3c) in its higher-latitude part and no structured aurora in its lower-latitude part

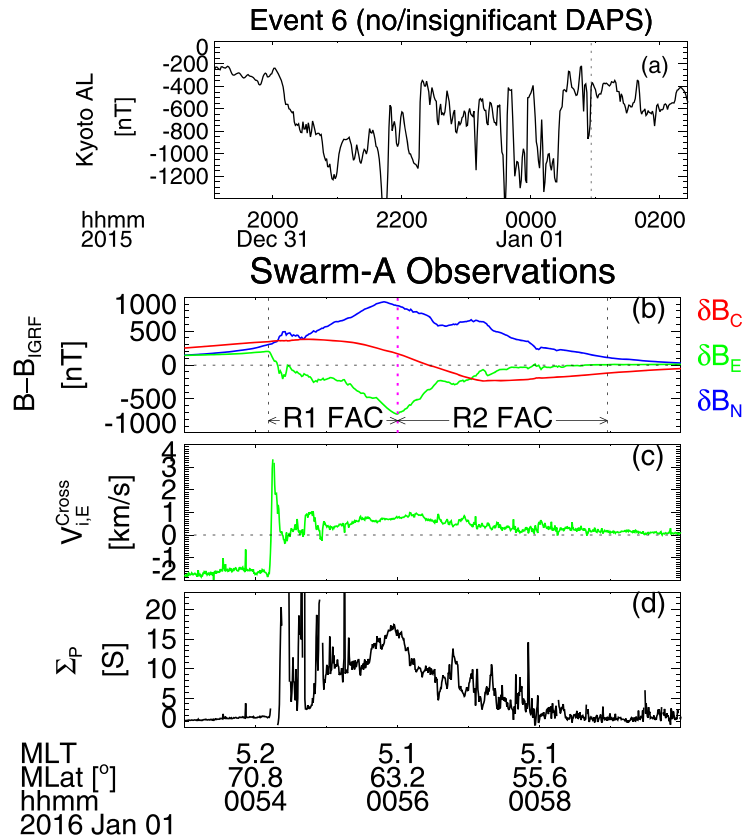


Figure 7. Swarm flying over the dawnside auroral zone without a DAPS. Panels (a), (b), and (d) are presented in the same way as Figures 4a, 4i, and 4k, respectively. (c) Cross-track ion bulk flow (positive eastward).

(Figure 1b; all SSUSI images in this paper are on the same color scale). The dim, discrete arcs correspond to the structured precipitation features (many inverted-Vs) from ~ 1332 to $1333:48$ UT in Figure 5g. In DMSP-16's in situ observation, the structured precipitation coincides with a gradual drop in δB_E from $1332:53$ to $1333:48$ UT in Figure 5c, both suggesting that the R1 current occupies the latitude range between the first two vertical dotted lines in Figure 5c (see Ohtani et al., 2010). The poleward boundary of the R1 current is near the poleward edge of the plasma sheet (indicated by the abrupt change in ion precipitation at $1332:43$ UT in Figure 5f). Equatorward of the R1 current, there is a gradual increase in δB_E from $1333:48$ to $1335:13$ UT (Figure 5c) denoting the R2 current, which coincides with unstructured precipitation (Figure 5f). Near the boundary between R1 and R2 FACs (magenta dotted line in Figure 5c), there is no steep gradient in the eastward flow (Figure 5d). The flow profile follows that of δB_E (see also Sugiura et al., 1982). Correspondingly, the inferred Pederson conductance (Figure 5e) does not change across the boundary between R1 and R2 currents. This is caused by lack of a strong, discrete arc in the R2 current range (Figure 5b), which should be typical during quiet times.

Figure 6 displays another low-activity interval on 13 May 2013 when AL is approximately -20 nT (vertical dashed line in Figure 6a) and DMSP-16 transects the auroral zone from ~ 4.7 MLT. This event (Event 5; ~ 1511 UT) has better-defined R1 and R2 currents (i.e., the corresponding drop and increase in Figure 6b, which are indicated by vertical dotted lines, are more monotonic) than those in Event 4. These are possibly related to the substorm at ~ 1700 UT ($AL = \sim -300$ nT). Because it has a low $|AL|$, ~ 1511 UT may be the early growth phase of that substorm. Although weak, convection may have already started and leads to well-defined R1 and R2 currents. The eastward flow (Figure 6c) shows a peak near the boundary between the R1 and R2 currents (the magenta dotted line in Figure 6b), but the flow profile is very different from that of DAPS. According to Figures 2e, 3d, and 4j, when DAPS occur, the eastward flow within the R2 current range (even when the R2 current density is large; i.e., when the rise of δB_E is steep) is much slower than that poleward of the R2 current. In Figure 6b, however, the flow is significant within the R2 current range, and

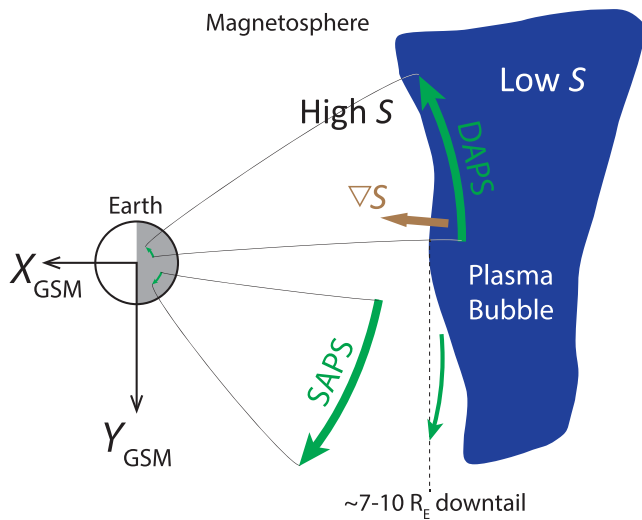


Figure 8. A schematic illustrating a late-stage plasma bubble (blue area) following the idea of Wang, Gkioulidou, et al. (2018) (see the $T = 15$ min column in their Figure 3). S = flux tube entropy. Green arrows = magnetospheric plasma flows, including the footprints of DAPS and SAPS in the equatorial plane.

the flow gradient is much smoother than that of DAPS. The flow just follows the variation in δB_E . The derived Pederson conductance (Figure 6d) does not increase with decreasing latitude across the boundary between R1 and R2 currents. We cannot confirm the conductance profile with an auroral image (there are no data for this interval), but the electron precipitation in Figure 6e resembles that in Figure 5e—there is no clear inverted-V structure, and thus no discrete arc, near the local time that DMSP-16 travels. Even if this is the growth phase of a substorm, the weak convection has apparently not accumulated enough pressure in the plasma sheet to lead to DAPS.

4.3.2. Absence of DAPS During Active Times

Although we expect DAPS to appear during active times, we find an event in which DAPS is absent or at most insignificant (Event 6; Figure 7). Around 0056 UT, 1 January 2016, Swarm-A transects the auroral zone at ~ 5.1 MLT when $AL = \sim -400$ nT (Figure 7a). Many eastward flow peaks (Figure 7c) appear within the ranges of the R1 and R2 currents (the ranges are marked by the vertical dotted lines in Figure 7b), but we cannot confidently call any of them a DAPS. Most of the peaks are at wrong locations (e.g., the two strong flows within the poleward part of R1 current). Although the flow peak near the boundary between the R1 and R2 currents (flow peak at $\sim 0056:15$ UT) has a gradient equatorward of it, the gradient leads to a much smaller flow change (relative to the flow peak value)

than did the DAPS' gradient in Events 1 to 3, so the flow peak is at most a weak DAPS. The lack of DAPS during such an active time may have resulted from too much activity— AL has been ≤ -200 nT for >6 hr (Figure 7a) before the Swarm observations, and it reached $\leq -1,000$ nT many times. At the time of Swarm observations, the Dst index is approximately -110 nT, indicating a moderate magnetic storm. These activities may have lit the entire auroral zone (from the polar cap to the equatorward edge of the R2 current), so a significant conductivity gradient is absent from the R1/R2 boundary (the conductivity is high everywhere). This absence is expected to prohibit a clear DAPS.

5. Discussion and Conclusions

Although a larger-scale study is needed for confirmation, the events we examined lead us to suggest that DAPS have the following fundamental features:

1. As expected from our proposed mechanism (Figure 1), DAPS can arise during active conditions such as a substorm expansion phase and after an auroral streamer appears (corresponding to fast flows in the magnetotail). We expect DAPS to exist during other types of active times.
2. When DAPS appear, the higher-latitude part of the R2 FAC contains a bright, discrete arc and a corresponding inverted-V structure. These indicate enhanced R2 current, consistent with the mechanism in Figure 1.
3. The latitudinal flow profile of DAPS indicates that its associated arc is of the “combination” type defined by Marklund (1984). This means that the flow profile is nearly equally contributed by polarization and current closure with FAC and conductivity effect, consistent with the mechanism in Figure 1.
4. The steep flow gradient of DAPS is near the boundary between R1 and R2 currents ($\leq 0.5^\circ$ equatorward of this boundary) and at the center of an inverted-V precipitation structure. This is understandable because the center of an inverted-V structure corresponds to the most intense FACs (e.g., Lyons, 1981), where the Pederson current, and thus the electric field and flow, should change most to feed the FAC. The flow equatorward of the steep gradient is much slower than that poleward of this boundary.
5. During quiet times when there is no bright arc or inverted-V structure in the expanse of R2 current (indicating that the R2 current is not enhanced), DAPS is absent from the dawnside auroral zone.
6. If the geomagnetic activity level is too high (or immediately after it was too high), the entire auroral zone may get high conductivity. The lack of conductivity difference between R1 and R2 will suppress DAPS.
7. In one event, we observed enhanced upward ion flow associated with DAPS.

As mentioned in sections 1 and 2, flows that are possibly DAPS have been reported in previous studies (Aikio et al., 2018; Jiang et al., 2015; Liu et al., 2018; Ziesolleck et al., 1983; Zou, Lyons, Nicolls, et al., 2009). We briefly discuss a few of them below, which can either support or complement our arguments.

Zou, Lyons, Nicolls, et al. (2009) observed enhancements of an eastward flow in the dawn convection cell and SAPS associated with a substorm westward traveling surge (Akasofu et al., 1965). They explained the flow enhancements with a mechanism like that in Figure 1, so their observed eastward flow may be a DAPS, although we cannot determine from their observation whether the flow has a steep gradient. This study suggests that DAPS may result from a westward traveling surge, a strong upward FAC the eastward part of which belongs to the R2 current.

Aikio et al. (2018) observed an eastward fast flow during a substorm expansion phase, coexisting with a discrete arc. Although they did not show the flow's relative location to the R1 and R2 currents, its latitudinal profile indicates that it is likely a DAPS. They found the electric field within the 1.5°-wide (in latitude) flow completed a significant part (41%) of the substorm-time potential drop in the dawn cell (the return flow region covers ~10° latitude), supporting our idea that DAPS partially results from the need of completing the potential drop (see section 2).

Although the DAPS events in substorm time in our paper both occurred during the expansion phase, likely DAPS also appeared during other phases of the substorm. A growth phase example is reported by Jiang et al. (2015). Their Figure 1A(i) showed an observation of eastward flow shear (equivalent to a steep gradient in southward electric field) at 2.4 MLT near the boundary between the R1 and R2 currents. Their flow gradient is not as steep as those shown in Figures 2 through 4, so their flow might be a developing DAPS. Their event is associated with a growth phase arc: a discrete arc with an inverse-V precipitation region, but not as significant as the arcs in Figures 2 through 4. We expect DAPS to appear in the late growth phase because the enhanced steady convection of this phase can build up pressure near the inner edge of the plasma sheet (Wing et al., 2007), which leads to enhanced R2 currents. A DAPS example during substorm recovery phase is in Liu et al. (2018) (see their Figures 1g and 2j, which are DAPS during substorm expansion and recovery phases, respectively). Their events were observed at ~2 MLT, when the poleward part of the R2 current contained a bright discrete arc.

Considering previous studies and our events, DAPS has been observed within 0–1, 2–3, and 5–6 MLT. Thus, DAPS is a common feature of the dawn convection cell.

5.1. Differences Between DAPS and Other Ionospheric Flows

As part of the ionospheric convection, DAPS may be confused with other ionospheric flows. Here we compare it with other types of flows.

5.1.1. Background Convection Vs. DAPS

As an eastward flow located in the dawnside return-flow region, the DAPS flows in the same direction as the background convection. What differentiates DAPS from the background convection, or further, an enhanced background convection, is the DAPS' unique flow profile as a function of latitude. The DAPS shows a steep flow gradient near the boundary between R1 and R2 currents, whereas the background convection flow (whether enhanced or not) is expected to vary more smoothly with latitude (e.g., Figure 5d). The reason for this profile difference is the underlying mechanism. The background flow increases as part of the enhanced large-scale M-I convection. The DAPS, however, arises only after the enhanced convection (either large-scale or BBFs) leads to enhanced R2 current (see Figure 1). The enhanced electron precipitation within the enhanced R2 current leads to a stark conductivity gradient between the R1 and R2 current regions in the ionosphere. This difference, combined with the Pederson current required by the enhanced R2 current, gives rise to the DAPS' steep electric field, and thus a flow gradient.

5.1.2. BCBF Vs. DAPS

Archer et al. (2017) defined a BCBF as a flow between the upward and downward Birkeland currents. Statistically, a BCBF in the postmidnight sector is hundreds of kilometers wide (i.e., covering several degrees of latitude), has an eastward flow peak at the boundary between R1 and R2 currents, and a typical peak velocity of >1 km/s. DAPS, represented by Events 1–3, clearly satisfy BCBF's definition and statistical features. Although the statistics of Archer et al. (2017) are for “quiet” conditions, DAPS (expected during active time) must have contributed to their results (the orange curve in their Figure 2 is a DAPS, although they did not

discuss it). This is because their definition of “quiet” is $AE < 200$ nT, which cannot exclude weak substorms and solitary BBFs (the case for our Event 3).

On the other hand, not all BCBFs are DAPS. Our Events 4 through 6 are BCBFs—they have flow peaks at the boundary between upward and downward. They also have other typical signatures of BCBFs—they are several degrees wide in latitude and one of them (Event 6) exceeds 1 km/s. However, as we explained in the previous sections, they are not DAPS.

5.1.3. SAPS Vs. DAPS

Although both result from the R2 current-required Pederson current, SAPS and DAPS have an essential difference in addition to their apparent differences in direction and location. This essential difference lies in the nature of the low conductivity region that the streams are associated with. The low conductivity region giving rise to SAPS is the midlatitude trough. This trough results from large-scale convection (Spiro et al., 1978), so it is already present before SAPS appear. The trough's conductivity is much lower than that in the auroral oval (e.g., Sharp, 1966). On the other hand, the DAPS resides within the auroral oval. The lower-latitude part of the postmidnight oval gets its conductivity drastically increased where the R2 current intensifies; this will leave the higher-latitude part of the oval as having relatively low conductivity (although it is still higher than the conductivity in nonsunlit regions outside the oval). This relatively low conductivity region will have to accommodate a large potential drop to complete the cross-tail potential drop in the return-flow region. This is because the lower-latitude part of the auroral oval has too high conductivity to accommodate a significant portion of the cross-tail potential drop. The potential drop (and thus electric field) in the relatively low conductivity region gives rise to DAPS, whereas SAPS arise in an absolutely low conductivity trough. Eventually, DAPS may create a high-latitude trough (see the next section), but this trough do not have to precede DAPS.

5.2. The Importance of DAPS

A DAPS is associated with a strong electric field that can heat the ionosphere via Joule heating (Cole, 1962b). One indicator of ionospheric Joule heating is enhanced upward ion flow (e.g., Strangeway, 2005; Winser et al., 1989), which we observed in Event 3 (Figure 4j). Such flow is a statistical feature of BCBFs in Archer et al. (2017); the statistics contains contributions from DAPS. Another indicator is ion temperature increase. This is also a statistical feature of BCBFs (Archer et al., 2017) and has been observed with likely DAPS (Aikio et al., 2018; Opgenoorth et al., 1990). By heating the ionosphere, DAPS should increase the recombination rate of the local plasma (Banks et al., 1974; Schunk et al., 1976) and create a trough of low plasma density. Supporting this speculation, Figure 4l shows a plasma density drop at the same location as the DAPS. (The density drop is not very significant at the ~ 450 km Swarm altitude because this altitude is considerably above the major site of Joule heating—the 100–200 km-high E and lower F region (Cole, 1962a). In addition, the heating lifts denser plasma from lower altitude to Swarm's altitude, reducing the significance of the density drop observed by Swarm. The even-higher DMSP does not observe any density drop at DAPS latitude. Also, Swarm and DMSP are too high to observe ion temperature enhancement due to DAPS' Joule heating.) More significant density drop associated with likely DAPS has been observed at lower altitudes (Opgenoorth et al., 1990). Considering the DAPS' location, the trough it may lead to is the high-latitude trough (see Rodger et al., 1992, and references therein), whose relationship to ionospheric fast flows has been recognized (e.g., Ma et al., 2000; Williams & Jain, 1986). Especially, observations in the post-midnight sector have associated the high-latitude trough with fast eastward flows (Vanhamäki et al., 2016; Voiculescu et al., 2016; Zou et al., 2013); the DAPS is also a fast eastward flow. The high-latitude trough usually appears during substorm time (Ma et al., 2000; Zou et al., 2013) when we also expect DAPS to arise. When DAPS reduces plasma density, the local conductivity decreases. This further enhances the electric field (if the local Pederson current needs to be maintained) and thus DAPS, which in-turn strengthens the trough. This possible mutual enhancement between the DAPS and the high-latitude trough is similar to that between SAPS and the midlatitude trough (Anderson et al., 1993). Eventually, the DAPS and trough may reach a dramatic level and significantly impact not only the ionosphere but also the dynamics and composition of the thermosphere. This possibility requires future investigation.

A DAPS may also impact the magnetosphere. With its major part within the lower-latitude portion of the R1 current, the equatorial footprint of a DAPS' electric field is in the plasma sheet tailward of $X_{GSM} = \sim -8 R_E$ (Liu et al., 2016). This electric field will modify the electric potential distribution, and thus convection of cold

magnetospheric plasma here. The modified potential distribution will also affect the drift of energetic particles, as SAPS does to inner magnetospheric particles (Lejosne et al., 2018). Because DAPS peaks near the boundary between R1 and R2 currents, its electric field will impact one region most—the transition region between dipole-like and tail-like magnetic fields (at 7–12 R_E downtail). This region is the most important for energy conversion during active events (e.g., substorms).

A DAPS may lead to instabilities in the M-I system. The steep flow gradient of DAPS is a shear that may cause Kelvin-Helmholtz (KH) instability. If the DAPS results from a BBF, its peak maps to a low-entropy region created by stopped BBF (Wang, Gkioulidou, et al., 2018). This region is also known as a late-stage plasma bubble (Chen & Wolf, 1993; Yang et al., 2011) or dipolarizing flux bundle (Liu et al., 2014; Liu, Angelopoulos, Zhou, et al., 2013). The bubble has lower thermal pressure and larger magnetic field, and thus lower flux tube entropy than the ambient plasma. At the earthward boundary of this bubble, where DAPS' flow shear maps to, lies a strong earthward gradient of flux tube entropy (Figure 8). This gradient is interchange unstable (e.g., Xing & Wolf, 2007), and when combined with the flow shear, can lead to hybrid KH/interchange instability (Yamamoto, 2009). One possible result of DAPS-caused instability is the omega band, an eastward-traveling curvy auroral form in the postmidnight-to-dawn sector (Akasofu & Kimball, 1964). This causality is supported by observations of Liu et al. (2018), which showed that Omega bands almost always coexist with DAPS. Proposed mechanisms for Omega band generation include KH instability (Rostoker & Samson, 1984), BBF-driving (Henderson et al., 2002; Weygand et al., 2015), and hybrid KH/interchange instability (Yamamoto, 2011). They, as we have suggested, are either the cause or a result of DAPS. Omega bands, which cause significant (up to ~1,000 nT) changes to the geomagnetic field (Jorgensen et al., 1999), are the major dynamic structures in the postmidnight-to-dawn sector. This means DAPS, the potential driver of Omega bands, is also important for this sector.

Because of DAPS' potential importance in the M-I-T system, incorporating it into global models of the system may greatly improve them. Given its importance, DAPS deserves more future studies. To determine how DAPS impact the magnetosphere, we must observe their magnetospheric counterparts in situ as was done for SAPS' counterparts (Maynard et al., 1980; Puhl-Quinn et al., 2007).

Appendix A: Equations That Control the Auroral Ionosphere

We may understand most phenomena discussed in this paper as consequences of current continuity:

$$\frac{\partial j_N}{\partial l_N} + \frac{\partial j_E}{\partial l_E} + \frac{\partial j_{\parallel}}{\partial l_{\parallel}} \approx \frac{\partial j_N}{\partial l_N} + \frac{\partial j_E}{\partial l_E} + \frac{\partial j_C}{\partial l_C} = 0, \quad (\text{A1})$$

where j_{\parallel} is the FAC density (positive downward); j_N and j_E are the north-south and east-west components of the horizontal current density, respectively (positive northward and eastward, respectively); and j_C is the vertical current density (positive downward). Integrating Equation A1 from the bottom to the top of the ionosphere, we have

$$-j_{\parallel}^{\text{top}} \approx \frac{\partial J_N}{\partial l_N} + \frac{\partial J_E}{\partial l_E}, \quad (\text{A2})$$

where J is the height-integrated horizontal current density (unit: A/m) and $j_{\parallel}^{\text{top}}$ is the FAC density at the top of the ionosphere (note that FAC density vanishes at the bottom of the ionosphere). Because the postmidnight-to-dawn sector is less deformed (i.e., active structures perturbing the current sheet topology) than the pre-midnight sector even during active time, both the R1 and R2 FACs, which control the electrodynamics of the auroral zone, can be approximated as vertical current sheets whose normal directions are north-south. Under this approximation, the auroral ionosphere is a 2-dimensional system (i.e., the north-south and up-down dimensions) with little variation in the east-west direction. Equation A2 thus becomes

$$-j_{\parallel}^{\text{top}} \approx \frac{\partial J_N}{\partial l_N} = \frac{\partial (J_N^P + J_N^H)}{\partial l_N}, \quad (\text{A3})$$

where J^P and J^H are the height-integrated Pederson and Hall currents, respectively. The north-south Hall current is proportional to the east-west electric field. In the return-flow region (which covers the auroral

oval), the east-west electric field is much smaller than the north-south electric field E_N (see the azimuthal flow lines in Figure 1e, which correspond to north-south electric field). Because the Pederson current J_N^P is proportional to the north-south electric field, it should be much larger than J_N^H . Equation A3 then becomes

$$-J_{\parallel}^{\text{top}} \approx \frac{\partial J_N^P}{\partial l_N} = \frac{\partial(\Sigma_P E_N)}{\partial l_N}, \quad (\text{A4})$$

where Σ_P is the height-integrated Pederson conductivity. From this equation we can estimate the height-integrated Pederson conductivity following the method of Archer and Knudsen (2018). In the northern hemisphere, we integrate Equation A4 toward the north and get

$$J_N^P - J_{N0}^P \approx \int_{l_{N0}}^{l_N} J_{\parallel}^{\text{top}} dl_N \approx \frac{\delta B_E - \delta B_{E0}}{\mu_0}, \quad (\text{A5})$$

where the subscript “0” denotes the equatorward boundary of the R2 current. The Pederson current \mathbf{J}^P is related to the electric field via $\mathbf{J}^P = \Sigma_P \mathbf{E}$. Because we have assumed that the eastward flow, and thus E_N , vanishes equatorward of the R2 FAC, $J_{N0}^P = 0$, we have from Equation A5

$$\Sigma_P = \frac{\delta B_E - \delta B_{E0}}{\mu_0 E_N}, \quad (\text{A6})$$

where $E_N = V_C B_E - V_E B_C \approx -V_E B_C$ (C is the vertically downward direction). The latter approximate equation has assumed $|V_C|$ to be smaller than or of the same order as the magnitude as $|V_E|$, considering that B_C is much larger than B_E in the auroral zone. Equation A6 also applies to the southern hemisphere. We estimate Σ_P only when $\Delta B_E - \Delta B_{E0}$ and E_N have the same sign because the conductivity can only be positive. To avoid singularities, we also omit computing Σ_P when E_N is near zero.

Acknowledgments

Work at UCLA has been supported by Air Force MURI grant AFOSR FA9559-16-1-0364 and NASA contract NAS5-02099. We thank Y. Nishimura and Yuzhang Ma for useful discussion and Judith Hohl for editing. We thank the DMSF, Swarm, THEMIS, Kyoto indices, and SuperMAG teams for providing data. We are grateful to the University of Calgary Swarm EFI team members (Johnathan Burchill, Levan Lomidze) for their assistance in processing and evaluating the Swarm cross-track ion drift data. The data used in this paper are publicly available at the Madrigal site (<http://cedar.openmadrigal.org/>), the Swarm FTP site (<ftp://swarm-diss.eo.esa.int/>), the THEMIS data center (<http://themis.ssl.berkeley.edu/data/themis/>), the SSUSI data center (<https://ssusi.jhuapl.edu/>), and the World Data Center for Geomagnetism, Kyoto (<http://wdc.kugi.kyoto-u.ac.jp/>).

References

- Aikio, A. T., Vanhamäki, H., Workayehu, A. B., Virtanen, I. I., Kauristie, K., Juusola, L., et al. (2018). Swarm satellite and EISCAT radar observations of a plasma flow channel in the auroral oval near magnetic midnight. *Journal of Geophysical Research: Space Physics*, 123, 5140–5158. <https://doi.org/10.1029/2018ja025409>
- Akasofu, S.-I. (1964). The development of the auroral substorm. *Planetary and Space Science*, 12, 273–282. [https://doi.org/10.1016/0032-0633\(64\)90151-5](https://doi.org/10.1016/0032-0633(64)90151-5)
- Akasofu, S.-I., & Kimball, D. S. (1964). The dynamics of the aurora—I. *Journal of Atmospheric and Terrestrial Physics*, 26(2), 205–211. [https://doi.org/10.1016/0021-9169\(64\)90147-3](https://doi.org/10.1016/0021-9169(64)90147-3)
- Akasofu, S.-I., Kimball, D. S., & Meng, C.-I. (1965). The dynamics of the aurora—II westward traveling surges. *Journal of Atmospheric and Terrestrial Physics*, 27(2), 173–187. [https://doi.org/10.1016/0021-9169\(65\)90114-5](https://doi.org/10.1016/0021-9169(65)90114-5)
- Anderson, P. C., Hanson, W. B., Heelis, R. A., Craven, J. D., Baker, D. N., & Frank, L. A. (1993). A proposed production model of rapid subauroral ion drifts and their relationship to substorm evolution. *Journal of Geophysical Research*, 98(A4), 6069–6078. <https://doi.org/10.1029/92ja01975>
- Angelopoulos, V., Baumjohann, W., Kennel, C. F., Coroniti, F. V., Kivelson, M. G., Pellat, R., et al. (1992). Bursty bulk flows in the inner central plasma sheet. *Journal of Geophysical Research*, 97(A4), 4027–4039. <https://doi.org/10.1029/91JA02701>
- Archer, W. E., & Knudsen, D. J. (2018). Distinguishing subauroral ion drifts from Birkeland current boundary flows. *Journal of Geophysical Research: Space Physics*, 123, 819–826. <https://doi.org/10.1002/2017ja024577>
- Archer, W. E., Knudsen, D. J., Burchill, J. K., Jackel, B., Donovan, E., Connors, M., & Juusola, L. (2017). Birkeland current boundary flows. *Journal of Geophysical Research: Space Physics*, 122(4), 4617–4627. <https://doi.org/10.1002/2016ja023789>
- Banks, P. M., Schunk, R. W., & Raitt, W. J. (1974). NO^+ and O^+ in the high latitude F-region. *Geophysical Research Letters*, 1(6), 239–242. <https://doi.org/10.1029/GL001i006p00239>
- Baumjohann, W. (1982). Ionospheric and field-aligned current systems in the auroral zone: A concise review. *Advances in Space Research*, 2(10), 55–62. [https://doi.org/10.1016/0273-1177\(82\)90363-5](https://doi.org/10.1016/0273-1177(82)90363-5)
- Birn, J., & Hesse, M. (2013). The substorm current wedge in MHD simulations. *Journal of Geophysical Research: Space Physics*, 118, 3364–3376. <https://doi.org/10.1002/jgra.50187>
- Brüning, K., & Goertz, C. K. (1986). Dynamics of a discrete auroral arc. *Journal of Geophysical Research*, 91(A6), 7057. <https://doi.org/10.1029/JA091iA06p07057>
- Brüning, K., Wilhelm, K., & Goertz, C. K. (1985). Why does the perpendicular electric field increase at the edge of auroral arcs? *Advances in Space Research*, 5(4), 79–82. [https://doi.org/10.1016/0273-1177\(85\)90119-X](https://doi.org/10.1016/0273-1177(85)90119-X)
- Chen, C. X., & Wolf, R. A. (1993). Interpretation of high-speed flows in the plasma sheet. *Journal of Geophysical Research*, 98, 21409. <https://doi.org/10.1029/93JA02080>
- Cole, K. D. (1962a). A source of energy for the ionosphere. *Nature*, 194(4823), 75–75. <https://doi.org/10.1038/194075a0>
- Cole, K. D. (1962b). Joule heating of the upper atmosphere. *Australian Journal of Physics*, 15(2), 223. <https://doi.org/10.1071/PH620223>
- Dungey, J. W. (1961). Interplanetary magnetic field and the auroral zones. *Physical Review Letters*, 6, 47–48. <https://doi.org/10.1103/PhysRevLett.6.47>
- Evans, J. V., Holt, J. M., Oliver, W. L., & Wand, R. H. (1980). Millstone hill incoherent scatter observations of auroral convection over $60^\circ \leq \Lambda \leq 75^\circ$. Initial results. *Journal of Geophysical Research*, 85(A1), 41–54. <https://doi.org/10.1029/JA085iA01p00041>

- Foster, J. C. (1983). An empirical electric field model derived from Chatanika radar data. *Journal of Geophysical Research*, *88*(A2), 981. <https://doi.org/10.1029/JA088iA02p00981>
- Foster, J. C., & Vo, H. B. (2002). Average characteristics and activity dependence of the subauroral polarization stream. *Journal of Geophysical Research*, *107*(A12). <https://doi.org/10.1029/2002ja009409>
- Gallardo-Lacourt, B., Nishimura, Y., Lyons, L. R., Mishin, E. V., Ruohoniemi, J. M., Donovan, E. F., et al. (2017). Influence of auroral streamers on rapid evolution of ionospheric SAPS flows. *Journal of Geophysical Research: Space Physics*, *122*, 12406–12420. <https://doi.org/10.1002/2017ja024198>
- Galperin, Y. I., Ponomarov, Y. N., & Zosinova, A. G. (1973). Direct measurements of ion drift velocity in the upper atmosphere during a magnetic storm, (11), 273.
- Gjerloev, J. W. (2009). A global ground-based magnetometer initiative. *Eos, Transactions American Geophysical Union*, *90*(27), 230. <https://doi.org/10.1029/2009EO270002>
- Gjerloev, J. W. (2012). The SuperMAG data processing technique: TECHNIQUE. *Journal of Geophysical Research*, *117*(A9), A09213. <https://doi.org/10.1029/2012JA017683>
- Gkioulidou, M., Wang, C.-P., Lyons, L. R., & Wolf, R. A. (2009). Formation of the Harang reversal and its dependence on plasma sheet conditions: Rice convection model simulations. *Journal of Geophysical Research*, *114*. <https://doi.org/10.1029/2008ja013955>
- Harang, L. (1946). The mean field of disturbance of polar geomagnetic storms. *Journal of Geophysical Research*, *51*(3). <https://doi.org/10.1029/TE051i003p00353>
- Hardy, D. A., Holeman, E. G., Burke, W. J., Gentile, L. C., & Bounar, K. H. (2008). Probability distributions of electron precipitation at high magnetic latitudes: ELECTRON PRECIPITATION. *Journal of Geophysical Research*, *113*. <https://doi.org/10.1029/2007JA012746>
- Henderson, M. G., Kepko, L., Spence, H., Connors, M., Sigwarth, J., Frank, L. A., et al. (2002). The evolution of north-south aligned auroral forms into auroral torch structures: The generation of omega bands and Ps6 pulsations via flow bursts. In R. M. Winglee (Ed.) (pp. 169–174). Presented at the the Sixth International Conference on Substorms, University of Washington, Seattle, Washington.
- Heppner, J. P. (1977). Empirical models of high-latitude electric fields. *Journal of Geophysical Research*, *82*(7), 1115–1125. <https://doi.org/10.1029/JA082i007p01115>
- Iijima, T., & Potemra, T. A. (1976). The amplitude distribution of field-aligned currents at northern high latitudes observed by Triad. *Journal of Geophysical Research*, *81*(13), 2165–2174. <https://doi.org/10.1029/JA081i013p02165>
- Jaggi, R. K., & Wolf, R. A. (1973). Self-consistent calculation of the motion of a sheet of ions in the magnetosphere. *Journal of Geophysical Research*, *78*(16), 2852–2866. <https://doi.org/10.1029/JA078i016p02852>
- Jiang, F., Kivelson, M. G., Strangeway, R. J., Khurana, K. K., & Walker, R. (2015). Ionospheric flow shear associated with the preexisting auroral arc: A statistical study from the FAST spacecraft data. *Journal of Geophysical Research: Space Physics*, *120*, 5194–5213. <https://doi.org/10.1002/2013ja019255>
- Jorgensen, A. M., Spence, H. E., Hughes, T. J., & McDiarmid, D. (1999). A study of omega bands and Ps6 pulsations on the ground, at low altitude and at geostationary orbit. *Journal of Geophysical Research*, *104*(A7), 14705–14715. <https://doi.org/10.1029/1998ja900100>
- Knudsen, D. J., Burchill, J. K., Buchert, S. C., Eriksson, A. I., Gill, R., Wahlund, J. E., et al. (2017). Thermal ion imagers and Langmuir probes in the Swarm electric field instruments. *Journal of Geophysical Research: Space Physics*, *122*, 2655–2673. <https://doi.org/10.1002/2016ja022571>
- Lejosne, S., Kunduri, B. S. R., Mozer, F. S., & Turner, D. L. (2018). Energetic electron injections deep into the inner magnetosphere: A result of the subauroral polarization stream (SAPS) potential drop. *Geophysical Research Letters*, *45*, 3811–3819. <https://doi.org/10.1029/2018gl077969>
- Liu, J., Angelopoulos, V., Chu, X., & McPherron, R. L. (2016). Distribution of Region 1 and 2 currents in the quiet and substorm time plasma sheet from THEMIS observations. *Geophysical Research Letters*, *43*, 7813–7821. <https://doi.org/10.1002/2016gl069475>
- Liu, J., Angelopoulos, V., Runov, A., & Zhou, X.-Z. (2013). On the current sheets surrounding dipolarizing flux bundles in the magnetotail: The case for wedgelets. *Journal of Geophysical Research: Space Physics*, *118*, 2000–2020. <https://doi.org/10.1002/jgra.50092>
- Liu, J., Angelopoulos, V., Zhou, X.-Z., & Runov, A. (2014). Magnetic flux transport by dipolarizing flux bundles. *Journal of Geophysical Research: Space Physics*, *119*, 909–926. <https://doi.org/10.1002/2013JA019395>
- Liu, J., Angelopoulos, V., Zhou, X.-Z., Runov, A., & Yao, Z. (2013). On the role of pressure and flow perturbations around dipolarizing flux bundles. *Journal of Geophysical Research: Space Physics*, *118*, 7104–7118. <https://doi.org/10.1002/2013JA019256>
- Liu, J., Lyons, L. R., Archer, W. E., Gallardo-Lacourt, B., Nishimura, Y., Zou, Y., et al. (2018). Flow shears at the poleward boundary of omega bands observed during conjunctions of Swarm and THEMIS ASI. *Geophysical Research Letters*, *45*, 1218–1227. <https://doi.org/10.1002/2017gl076485>
- Lomidze, L., Burchill, J. K., Knudsen, D. J., Kouznetsov, A., & Weimer, D. R. (2019). Validity study of the Swarm horizontal cross-track ion drift velocities in the high-latitude ionosphere. *Earth and Space Science*, *6*(3), 411–432. <https://doi.org/10.1029/2018EA000546>
- Lyons, L. R. (1981). Discrete aurora as the direct result of an inferred high-altitude generating potential distribution. *Journal of Geophysical Research*, *86*(A1). <https://doi.org/10.1029/JA086iA01p00001>
- Lyons, L. R., Nishimura, Y., Xing, X., Runov, A., Angelopoulos, V., Donovan, E., & Kikuchi, T. (2012). Coupling of dipolarization front flow bursts to substorm expansion phase phenomena within the magnetosphere and ionosphere. *Journal of Geophysical Research*, *117*, A02212. <https://doi.org/10.1029/2011JA017265>
- Ma, S. Y., Liu, P., & Schlegel, K. (2000). EISCAT observation of a high-latitude ionization trough associated with a reversed westward plasma flow. *Geophysical Research Letters*, *27*(20), 3269–3272. <https://doi.org/10.1029/2000gl000073>
- Marklund, G. (1984). Auroral arc classification scheme based on the observed arc-associated electric field pattern. *Planetary and Space Science*, *32*(2), 193–211. [https://doi.org/10.1016/0032-0633\(84\)90154-5](https://doi.org/10.1016/0032-0633(84)90154-5)
- Marklund, G., Sandahl, I., & Opgenoorth, H. (1982). A study of the dynamics of a discrete auroral arc. *Planetary and Space Science*, *30*(2), 179–197. [https://doi.org/10.1016/0032-0633\(82\)90088-5](https://doi.org/10.1016/0032-0633(82)90088-5)
- Maynard, N. C., Aggson, T. L., & Heppner, J. P. (1980). Magnetospheric observation of large sub-auroral electric fields. *Geophysical Research Letters*, *7*(11), 881–884. <https://doi.org/10.1029/GL007i011p00881>
- Maynard, N. C., Denig, W. F., & Burke, W. J. (1995). Mapping ionospheric convection patterns to the magnetosphere. *Journal of Geophysical Research*, *100*(A2), 1713. <https://doi.org/10.1029/94JA02626>
- Mende, S. B., Harris, S. E., Frey, H. U., Angelopoulos, V., Russell, C. T., Donovan, E., et al. (2008). The THEMIS array of ground-based observatories for the study of auroral substorms. *Space Science Reviews*, *141*(1-4), 357–387. <https://doi.org/10.1007/s11214-008-9380-x>
- Merayo, J. M. G., Jorgensen, J. L., Friis-Christensen, E., Brauer, P., Prindahl, F., Jorgensen, P. S., et al. (2008). The Swarm magnetometry package. In *Small Satellites for Earth Observation* (pp. 143–151). Netherlands: Springer. https://doi.org/10.1007/978-1-4020-6943-7_13

- Muldrew, D. B. (1965). *F*-layer ionization troughs deduced from Alouette data. *Journal of Geophysical Research*, 70(11), 2635–2650. <https://doi.org/10.1029/JZ070i011p02635>
- Nakamura, R., Baumjohann, W., Schödel, R., Brittnacher, M., Sergeev, V. A., Kubyskhina, M., et al. (2001). Earthward flow bursts, auroral streamers, and small expansions. *Journal of Geophysical Research*, 106(A6), 10791–10802. <https://doi.org/10.1029/2000JA000306>
- Nishida, A. (1979). Possible origin of transient dusk-to-dawn electric field in the nightside magnetosphere. *Journal of Geophysical Research*, 84(A7), 3409. <https://doi.org/10.1029/JA084iA07p03409>
- Nishimura, Y., Lyons, L. R., Zou, S., Angelopoulos, V., & Mende, S. B. (2010). Reply to comment by Harald U. Frey on “Substorm triggering by new plasma intrusion: THEMIS all-sky imager observations.”. *Journal of Geophysical Research*, 115, A12233. <https://doi.org/10.1029/2010JA016182>
- Ohtani, S., Wing, S., Newell, P. T., & Higuchi, T. (2010). Locations of night-side precipitation boundaries relative to R2 and R1 currents. *Journal of Geophysical Research*, 115, A10233. <https://doi.org/10.1029/2010ja015444>
- Opgenoorth, H. J., Hågström, I., Williams, P. J. S., & Jones, G. O. L. (1990). Regions of strongly enhanced perpendicular electric fields adjacent to auroral arcs. *Journal of Atmospheric and Terrestrial Physics*, 52(6–8), 449–458. [https://doi.org/10.1016/0021-9169\(90\)90044-N](https://doi.org/10.1016/0021-9169(90)90044-N)
- Paxton, L. J., Schaefer, R. K., Zhang, Y., Kil, H., & Hicks, J. E. (2018). SSUSI and SSUSI-Lite: Providing space situational awareness and support for over 25 years. *Johns Hopkins APL Technical Digest*, 34(3).
- Pontius, D. H., & Wolf, R. A. (1990). Transient flux tubes in the terrestrial magnetosphere. *Geophysical Research Letters*, 17, 49–52. <https://doi.org/10.1029/GL017i001p00049>
- Puhl-Quinn, P. A., Matsui, H., Mishin, E., Moukik, C., Kistler, L., Khotyaintsev, Y., et al. (2007). Cluster and DMSP observations of SAID electric fields. *Journal of Geophysical Research*, 112, A05219. <https://doi.org/10.1029/2006ja012065>
- Rich, F. J. (1984). Fluxgate magnetometer (SSM) for the Defense Meteorological Satellite Program (DMSP) Block 5D-2, flight 7. Tech. Rep. AFGL-TR-84-0225, Air Force Geophys. Lab., Hanscom Air Force Base, Mass.
- Rich, F. J., & Hairston, M. (1994). Large-scale convection patterns observed by DMSP. *Journal of Geophysical Research*, 99(A3), 3827. <https://doi.org/10.1029/93JA03296>
- Rodger, A. S., Moffett, R. J., & Quegan, S. (1992). The role of ion drift in the formation of ionisation troughs in the mid- and high-latitude ionosphere—A review. *Journal of Atmospheric and Terrestrial Physics*, 54(1), 1–30. [https://doi.org/10.1016/0021-9169\(92\)90082-v](https://doi.org/10.1016/0021-9169(92)90082-v)
- Rostoker, G., & Samson, J. C. (1984). Can substorm expansive phase effects and low frequency Pc magnetic pulsations be attributed to the same source mechanism? *Geophysical Research Letters*, 11(3), 271–274. <https://doi.org/10.1029/GL011i003p00271>
- Schunk, R. W., Banks, P. M., & Raitt, W. J. (1976). Effects of electric fields and other processes upon the nighttime high-latitude *F* layer. *Journal of Geophysical Research*, 81(19), 3271–3282. <https://doi.org/10.1029/JA081i019p03271>
- Sergeev, V. A., Angelopoulos, V., Gosling, J. T., Cattell, C. A., & Russell, C. T. (1996). Detection of localized, plasma-depleted flux tubes or bubbles in the midtail plasma sheet. *Journal of Geophysical Research*, 101(A5), 10817–10826. <https://doi.org/10.1029/96ja00460>
- Sharp, G. W. (1966). Midlatitude trough in the night ionosphere. *Journal of Geophysical Research*, 71(5), 1345–1356. <https://doi.org/10.1029/JZ071i005p01345>
- Spiro, R. W., Heelis, R. A., & Hanson, W. B. (1978). Ion convection and the formation of the mid-latitude *F* region ionization trough. *Journal of Geophysical Research*, 83(A9), 4255. <https://doi.org/10.1029/JA083iA09p04255>
- Spiro, R. W., Heelis, R. A., & Hanson, W. B. (1979). Rapid subauroral ion drifts observed by Atmosphere Explorer C. *Geophysical Research Letters*, 6(8), 657–660. <https://doi.org/10.1029/GL006i008p00657>
- Strangeway, R. J. (2005). Factors controlling ionospheric outflows as observed at intermediate altitudes. *Journal of Geophysical Research*, 110, A03221. <https://doi.org/10.1029/2004JA010829>
- Sugiura, M., Maynard, N. C., Farthing, W. H., Heppner, J. P., Ledley, B. G., & Cahill, L. J. Jr. (1982). Initial results on the correlation between the magnetic and electric fields observed from the DE-2 satellite in the field-aligned current regions. *Geophysical Research Letters*, 9, 985–988. <https://doi.org/10.1029/GL009i009p00985>
- Vanhamäki, H., Aikio, A., Voiculescu, M., Juusola, L., Nygrén, T., & Kuula, R. (2016). Electrodynamic structure of the morning high-latitude trough region: TROUGH ELECTRODYNAMICS. *Journal of Geophysical Research: Space Physics*, 121, 2669–2682. <https://doi.org/10.1002/2015JA022021>
- Vickrey, J. F., Livingston, R. C., Walker, N. B., Potemra, T. A., Heelis, R. A., Kelley, M. C., & Rich, F. J. (1986). On the current-voltage relationship of the magnetospheric generator at intermediate spatial scales. *Geophysical Research Letters*, 13(6), 495–498. <https://doi.org/10.1029/GL013i006p00495>
- Voiculescu, M., Nygrén, T., Aikio, A. T., Vanhamäki, H., & Pierrard, V. (2016). Postmidnight ionospheric troughs in summer at high latitudes: POSTMIDNIGHT HIGH-LATITUDE SUMMER TROUGHS. *Journal of Geophysical Research: Space Physics*, 121, 12171–12185. <https://doi.org/10.1002/2016JA023360>
- Wang, C.-P., Gkioulidou, M., Lyons, L. R., & Wolf, R. A. (2018). Spatial distribution of plasma sheet entropy reduction caused by a plasma bubble: Rice convection model simulations. *Journal of Geophysical Research: Space Physics*, 123, 3380–3397. <https://doi.org/10.1029/2018ja025347>
- Wang, C.-P., Xing, X., Liu, Y.-H., & Runov, A. (2018). A case study of connection between ground magnetic field perturbations and tail current sheet bursty flows at $X = -60 R_E$. *Journal of Geophysical Research: Space Physics*, 123, 1822–1833. <https://doi.org/10.1002/2017JA024972>
- Weygand, J. M., Kivelson, M. G., Frey, H. U., Rodriguez, J. V., Angelopoulos, V., Redmon, R., et al. (2015). An interpretation of spacecraft and ground based observations of multiple omega band events. *Journal of Atmospheric and Solar-Terrestrial Physics*, 133, 185–204. <https://doi.org/10.1016/j.jastp.2015.08.014>
- Wiens, R. G., & Rostoker, G. (1975). Characteristics of the development of the westward electrojet during the expansive phase of magnetospheric substorms. *Journal of Geophysical Research*, 80(16), 2109–2128. <https://doi.org/10.1029/JA080i016p02109>
- Williams, P. J. S., & Jain, A. R. (1986). Observations of the high latitude trough using EISCAT. *Journal of Atmospheric and Terrestrial Physics*, 48(5), 423–434. [https://doi.org/10.1016/0021-9169\(86\)90119-4](https://doi.org/10.1016/0021-9169(86)90119-4)
- Wing, S., Gjerloev, J. W., Johnson, J. R., & Hoffman, R. A. (2007). Substorm plasma sheet ion pressure profiles: SUBSTORM ION PRESSURE PROFILES. *Geophysical Research Letters*, 34. <https://doi.org/10.1029/2007GL030453>
- Winsor, K. J., Jones, G. O. L., Williams, P. J. S., & Lockwood, M. (1989). Observations of large field-aligned flows of thermal plasma in the auroral ionosphere. *Advances in Space Research*, 9(5), 57–63. [https://doi.org/10.1016/0273-1177\(89\)90341-4](https://doi.org/10.1016/0273-1177(89)90341-4)
- Wolf, R. A. (1970). Effects of ionospheric conductivity on convective flow of plasma in the magnetosphere. *Journal of Geophysical Research*, 75(25), 4677–4698. <https://doi.org/10.1029/JA075i025p04677>
- Xing, X., & Wolf, R. A. (2007). Criterion for interchange instability in a plasma connected to a conducting ionosphere: INTERCHANGE INSTABILITY CRITERION IN PLASMA SHEET. *Journal of Geophysical Research*, 112, A12209. <https://doi.org/10.1029/2007JA012535>

- Yamamoto, T. (2009). Hybrid Kelvin-Helmholtz/Rayleigh-Taylor instability in the plasma sheet: HYBRID KH/RT INSTABILITY IN PLASMA SHEET. *Journal of Geophysical Research*, *114*, A06207. <https://doi.org/10.1029/2008JA013760>
- Yamamoto, T. (2011). A numerical simulation for the omega band formation. *Journal of Geophysical Research*, *116*, A02207. <https://doi.org/10.1029/2010ja015935>
- Yang, J., Toffoletto, F. R., Wolf, R. A., & Sazykin, S. (2011). RCM-E simulation of ion acceleration during an idealized plasma sheet bubble injection. *Journal of Geophysical Research*, *116*, A05207. <https://doi.org/10.1029/2010JA016346>
- Ziesolleck, C., Baumjohann, W., Brüning, K., Carlson, C. W., & Bush, R. I. (1983). Comparison of height-integrated current densities derived from ground-based magnetometer and rocket-borne observations during the Porcupine F3 and F4 flights. *Journal of Geophysical Research*, *88*(A10), 8063. <https://doi.org/10.1029/JA088iA10p08063>
- Zou, S., Lyons, L. R., Nicolls, M. J., Heinselman, C. J., & Mende, S. B. (2009). Nightside ionospheric electrodynamics associated with substorms: PFISR and THEMIS ASI observations: IONOSPHERIC CONVECTION DURING SUBSTORM. *Journal of Geophysical Research*, *114*, A12301. <https://doi.org/10.1029/2009JA014259>
- Zou, S., Lyons, L. R., Wang, C. P., Boudouridis, A., Ruohoniemi, J. M., Anderson, P. C., et al. (2009). On the coupling between the Harang reversal evolution and substorm dynamics: A synthesis of SuperDARN, DMSP, and IMAGE observations. *Journal of Geophysical Research*, *114*(A1). <https://doi.org/10.1029/2008ja013449>
- Zou, S., Moldwin, M. B., Nicolls, M. J., Ridley, A. J., Coster, A. J., Yizengaw, E., et al. (2013). Electrodynamics of the high-latitude trough: Its relationship with convection flows and field-aligned currents. *Journal of Geophysical Research: Space Physics*, *118*, 2565–2572. <https://doi.org/10.1002/jgra.50120>